Electrocatalytic Activity and Structural Transformation of $Ca_2Sr_2Mn_2MO_{10-\delta}$ (M = Fe, Co)

Surendra B. Karki[a,⊥], Ram Krishna Hona[a,⊥], Farshid Ramezanipour[a,*]

[a]Department of Chemistry, University of Louisville, Louisville, Kentucky 40292, USA

*Corresponding author. Email: farshid.ramezanipour@louisville.edu, Phone: (502) 852-7061

ORCID: 0000-0003-4176-1386

⊥ These authors contributed equally to this work

Abstract

The structural transformation between $Ca_2Sr_2Mn_2FeO_{10-\delta}$ and $Ca_2Sr_2Mn_2CoO_{10-\delta}$ and the enhancement in electrocatalytic activity is reported. $Ca_2Sr_2Mn_2FeO_{10-\delta}$ has a structure where corner-sharing $(Mn/Fe)O_6$ octahedra form triple-layered stacks and Ca/Sr are located in spaces within and between the stacks. The incorporation of cobalt results in $Ca_2Sr_2Mn_2CoO_{10-\delta}$, which has a greater concentration of oxygen vacancies and a quazi one-dimensional structure, consisting of chains of CoO_6–MnO_6–MnO_6–CoO_6 polyhedra with distorted trigonal prismatic and octahedral geometry. Detailed investigation of the electrocatalytic activities of these materials indicates that these compounds are able to catalyze both half-reactions of water-splitting, namely hydrogen-evolution reaction (HER) and oxygen-evolution reaction (OER). $Ca_2Sr_2Mn_2CoO_{10-\delta}$ shows enhanced electrocatalytic properties compared with $Ca_2Sr_2Mn_2FeO_{10-\delta}$. The former material exhibits lower overpotential and greater electrochemically active surface area, as well as faster kinetics for both HER and OER processes.

Keywords: Crystal structures, Catalysis, Electrolysis, Water splitting

1. Introduction

Structural changes are often associated with variations in material properties. Even small changes in structure can have a significant impact on other attributes of a material. Examples of such effects are observed in Ruddlesden-Popper oxides (Figure 1), which are derivatives of perovskite oxides. They have the general formula $A_{n+1}B_nO_{3n+1}$ (n = 1, 2, 3), where A is usually a rare earth or alkaline earth metal, B is often a transition metal, and *n* represents the number of perovskite-type layers in each stack, consisting of corner-sharing BO_6 octahedra. When *n* = 1, the formula is simplified into A_2BO_4, which resembles the crystal structure of the fluoride K_2NiF_4.[1] Increasing the number of perovskite layers to *n* = 2 results in $A_3B_2O_7$, while *n* = 3 gives $A_4B_3O_{10}$, etc. Ultimately, when *n* approaches infinity, the structure transforms into a typical perovskite structure. Changes in properties of these materials can be achieved upon varying the A or B cations. For example, the structure of the Ruddlesden-Popper oxide $Ca_4Mn_3O_{10}$ changes significantly if calcium is replaced by strontium on the A site.[2] The crystal structure of $Ca_4Mn_3O_{10}$ is a typical Ruddlesden-Popper structure and consists of trilayer stacks of corner-sharing MnO_6 octahedra, with Ca residing in intra- and inter-stack spaces.[3] However, $Sr_4Mn_3O_{10}$ shows a $Cs_4Ni_3F_{10}$-type structure,[2] where there are Mn_3O_{12} units consisting of trimers of face sharing octahedra.[4] These trimeric Mn_3O_{12} units share apices to form two-dimensional layers. $Ca_4Mn_3O_{10}$ shows antiferromagnetic order below 122 K,[2] whereas $Sr_4Mn_3O_{10}$ undergoes a transition into long range antiferromagnetic order below 67 K.[5,6] On the other hand, a compound containing both calcium and strontium on A sites, $Sr_{1.15}Ca_{2.85}Mn_3O_{10-\delta}$, is a semiconductor and exhibits spin-glass like transition at low temperature.[7] Similarly, the incorporation of lanthanum results in $La_{3-3x}Sr_{1+3x}Mn_3O_{10}$ with significantly different magnetic properties.[5]

Another example of the effect of the A-site cations is the variation in properties between $La_4Co_3O_{10}$ and its Nd-analogue. $La_4Co_3O_{10}$ has a C-centered structure with space group *C*2/*m*.[8] At 840 K, this compound undergoes a structural phase transition from monoclinic to tetragonal. It also shows long-range antiferromagnetic order below $T_N \approx 13$ K.[8] The Nd-analogue, $Nd_4Co_3O_{10}$, on the other hand, has a crystal structure with space group $P2_1/a$ and shows long-range antiferromagnetic order below 15 K.[9]

Changes to the B-site cation can also result in variation of properties in Ruddlesden–Popper oxides $A_{n+1}B_nO_{3n+1}$. For example, replacing some of the manganese by niobium in $Ca_4Mn_3O_{10}$, results in $Ca_4Mn_{3-x}Nb_xO_{10}$ (x = 0 – 0.2) phases, which show an increase in both unit cell volume and octahedral distortion.[10] The doped samples display ferromagnetism-like behavior. A significant magnetoresistance effect is observed for the doped samples in comparison with the undoped material. Another example of the effect of B-site cation is the variation in symmetry when manganese in $Ca_4Mn_3O_{10}$ is partially replaced by iron, changing the *Pbca* space group into *I*4/*mmm*.[11]

Among various properties of oxide materials, their electrocatalytic properties are very attractive and there is a great potential for their application in areas such as water-splitting. The electrocatalytic water-splitting consists of two half-reactions, namely oxygen-evolution reaction (OER) and hydrogen-evolution reaction (HER). Some Ruddlesden–Popper oxides have been studied as water-splitting electrocatalysts. While some members of this family have good electrocatalytic performance,[12] many others show only modest activity. For example, the OER overpotential is 522 mV for $LaSr_3Fe_3O_{10-\delta}$ and 0.475 mV for $LaSr_3Co_2FeO_{10-\delta}$ in 0.1 M KOH.[13] There are also examples of HER electrocatalysts, such as $Sr_2LaCoMnO_7$ with overpotential of 612 mV in 0.5 M H_2SO_4,[14] and $SrLaCoO_{4-\delta}$ with overpotential of 541 mV in 1 M KOH.[15] Various

strategies have been used to enhance the electrocatalytic activity, most commonly by composite preparations. For example, a composite catalyst containing S-adsorbed Ruddlesden-Popper oxide $(Nd_{0.6}Sr_{0.4})_3((Co,Fe)_{0.85}Nb_{0.15})_2O_7$, metal sulfides, and hollow S-doped carbon fibers has been prepared,[16] giving OER overpotential of ~420 mV and HER overpotential of ~470 mV in 1 M KOH.[16] In the present study, we have shown the enhancement of electrocatalytic activity for both OER and HER through replacing iron in the Ruddlesden-Popper oxide $Ca_2Sr_2Mn_2FeO_{10-\delta}$ by cobalt to form $Ca_2Sr_2Mn_2CoO_{10-\delta}$, which has a 1-dimensional structure, consisting of infinite chains of face-sharing octahedra and trigonal prisms. While the magnetic properties of the latter material have been studied,[17] the electrocatalytic properties for water-splitting and the major impact of compositional and structural transformation on electrocatalytic activity of these materials have not been investigated.

2. Experimental

$Ca_2Sr_2Mn_2CoO_{10-\delta}$ and $Ca_2Sr_2Mn_2FeO_{10-\delta}$ were synthesized by solid state synthesis method using stoichiometric amounts of $CaCO_3$ (Alfa Aesar, 99.95%), $SrCO_3$ (Alfa Aesar, 99.95%), Mn_2O_3 (Alfa Aesar, 99.95%), Co_3O_4 (Alfa Aesar, 99.95%), and Fe_2O_3 (Alfa Aesar, 99.95%). Pellets of both samples were first calcined at 1200 ºC for 24 hours in air. After grinding and re-pelletizing, samples of $Ca_2Sr_2Mn_2CoO_{10-\delta}$ and $Ca_2Sr_2Mn_2FeO_{10-\delta}$ were sintered for 24 hours at 1300 and 1350 ºC, respectively. This step can also be done at 1300 °C for both materials, but the latter material would require additional refiring at 1300 °C. The heating and cooling rates were 100 °C/h. Powder X-ray diffraction with Cu Kα1 radiation (λ = 1.54056 Å) was employed for investigation of the structures of polycrystalline samples. The GSAS software[18] and EXPEGUI interface[19] were used for Rietveld refinements. High resolution field-emission scanning electron microscopy

(SEM) was utilized to examine the microstructure of the materials. Iodometric titration was performed for oxygen content determination[20-22] by dissolving 50 mg of the sample and excess KI (~2 g) in 100 mL of 1M HCl. 5 mL of the solution was then pipetted out, and iodine that had formed in the solution was titrated by 0.025 M $Na_2S_2O_3$. Near the end point of the titration, 0.2mL of a starch solution was added as an indicator. All steps were performed under an argon atmosphere. The solution was purged with argon for at least 3 hours to remove any dissolved oxygen. X-ray photoelectron spectroscopy (XPS) was done at room temperature using Al Kα radiation (1486.7 eV) to study the valence states of B site cations.

Electrocatalytic properties were measured in a three-electrode glass cell system. Catalyst electrode was prepared by dropcast method using a mixture of sample, nafion and carbon black. 35 mg of the sample and 7 mg of carbon powder were added to 20 µL of nafion and stirred for few minutes. 7 mL of THF was then added and stirred for few more minutes, followed by sonication for 5 minutes. 40 µL of the catalyst ink (in 10 µL increments) was loaded onto a glassy carbon (GC) electrode of 5 mm diameter (area 0.196 cm^2), and was dried in air overnight. Before starting each measurement, the electrolyte solution was bubbled with argon gas for at least 30 minutes. The glassy carbon (GC) electrode coated with the catalyst was used as working electrode, while an Ag/AgCl (in 3 M or saturated NaCl) was the reference electrode, and a carbon rod (for HER) or a platinum electrode (for OER) were used as counter electrode. The cyclic voltammetry (CV) profiles were recorded using a rotating disk electrode (RDE) at 1600 rpm with scan rate of 10 mV s^{-1} from 0 to 0.8 V vs Ag/AgCl. Resistance (R) was measured before each electrocatalytic experiment using potentiostatic electrochemical impedance spectroscopy (PEIS) in the frequency range of 100 KHz to 1 Hz. Then, the resulting potentials were converted into the reversible hydrogen electrode (RHE) after iR correction according to the following equation:

$E_{RHE} = E_{Ag/AgCl} + 0.059\ pH + E^{o}_{Ag/AgCl}$

where $E^{0}_{vs\ Ag/AgCl} = 0.21V$ for 3M NaCl and 0.197V for saturated NaCl for OER and HER measurements, respectively. Chronopotentiometry was used to study the stability of the catalysts in 0.1M and 1M KOH electrolytes for OER and HER, respectively, using a two-electrode method described in the literature.[23] The electrodes were fabricated by dropcasting 100 μL catalyst ink on 1 cm^2 nickel foam, followed by air drying overnight to obtain a total mass loading of ~ 1 mg/cm^2. Two such electrodes were prepared, which were sandwiched between gold leads attached to gold wires and separated by a glass fiber filter paper to prevent short circuiting and crossover.[24]

3. Results and Discussion

3.1. Crystal Structure

$Ca_2Sr_2Mn_2FeO_{10-\delta}$, forms the so-called Ruddlesden-Popper type structure with tetragonal *I*4/*mmm* space group, resembling $Ca_4Mn_2FeO_{10-\delta}$ and $Sr_4Mn_2FeO_{10-\delta}$.[11] Figure 1 shows the Rietveld refinement profile and crystal structure of $Ca_2Sr_2Mn_2FeO_{10-\delta}$, based on the same model as $Sr_4Mn_2FeO_{10-\delta}$.[11] The refined structural parameters are listed in Table 1. Its structure comprises corner-sharing units of $(Fe/Mn)O_6$ octahedra that form triple-layered stacks. The alkaline-earth metals Ca/Sr reside in spaces within and between the octahedral stacks. Considering the occurrence of oxygen-deficiencies in this compound, as indicated by iodometric titration and consistent with the presence of trivalent iron, some of the oxygen sites in the structure should be only partially occupied. Previous studies on similar materials using neutron diffraction[11] have indicated that vacancies appear on oxygen sites located within the stacks, namely O1 and O4 site in Figure 1b.

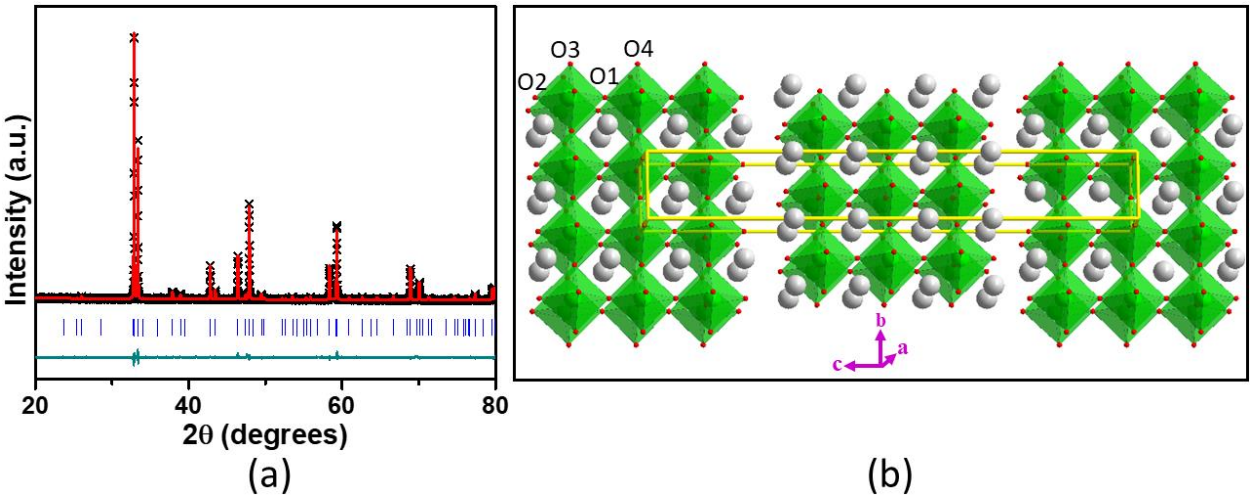

Figure 1. **(a)** Rietveld refinement profile for powder X-ray diffraction data of $Ca_2Sr_2Mn_2FeO_{10-\delta}$. Black crosses, red line, vertical tick marks and lower green line represent experimental data, the model, peak positions, and difference plot, respectively. **(b)** Crystal structure of $Ca_2Sr_2Mn_2FeO_{10-\delta}$, showing $(Fe/Mn)O_6$ octahedral units in green. Grey spheres represent Ca/Sr. Yellow lines show the unit cell.

Table 1. Refined structural parameters for $Ca_2Sr_2Mn_2FeO_{10-\delta}$ using powder X-ray diffraction data. Space group *I4/mmm,* a = 3.79541(2) Å, b = 3.79541(2) Å, c = 27.3699(2) Å, V = 394.267(7) $Å^3$, Rp=0.0231, wRp= 0.0304, χ^2 = 1.865

Elements	x	y	z	Multiplicity	Occupancy	Uiso
Ca1/Sr1	0	0	0.5711(1)	4	0.5/0.5	0.012(1)
Ca2/Sr2	0	0	0.7026(1)	4	0.5/0.5	0.029(2)
Mn1/Fe1	0	0	0	2	0.6667/0.3333	0.023(4)
Mn2/Fe2	0	0	0.1420(2)	4	0.6667/0.3333	0.020(1)
O1	0	0	0.0696(7)	4	0.8750	0.035(1)
O2	0	0	0.2112(4)	4	1	0.035(1)
O3	0	0.5	0.6399(4)	8	1	0.035(1)
O4	0	0.5	0.5	4	0.8750	0.035(1)

$Ca_2Sr_2Mn_2CoO_{10-\delta}$ forms a completely different structure, featuring 1-dimensioanl chains, consistent with a previous report.[17] Figure 2 shows the Rietveld refinement profile and crystal structure of $Ca_2Sr_2Mn_2CoO_{10-\delta}$, matching a previously reported model.[25] The refined structural parameters are listed in Table 2. The trigonal structure of $Ca_2Sr_2Mn_2CoO_{10-\delta}$ with space group *P*321 consists of chains of face-sharing polyhedra running along the *c*-axis.[17] The chains comprise an ordered arrangement of CoO_6–MnO_6–MnO_6–CoO_6, where two MnO_6 units alternate with a single unit of CoO_6. The MnO_6 polyhedra form distorted trigonal prismatic and octahedral

geometry, while the CoO_6 units form two types of trigonal prisms, one highly distorted and another close to the ideal geometry. The polyhedra in each chain are connected through face-sharing. The spaces between the one-dimensional chains are occupied by Ca and Sr.

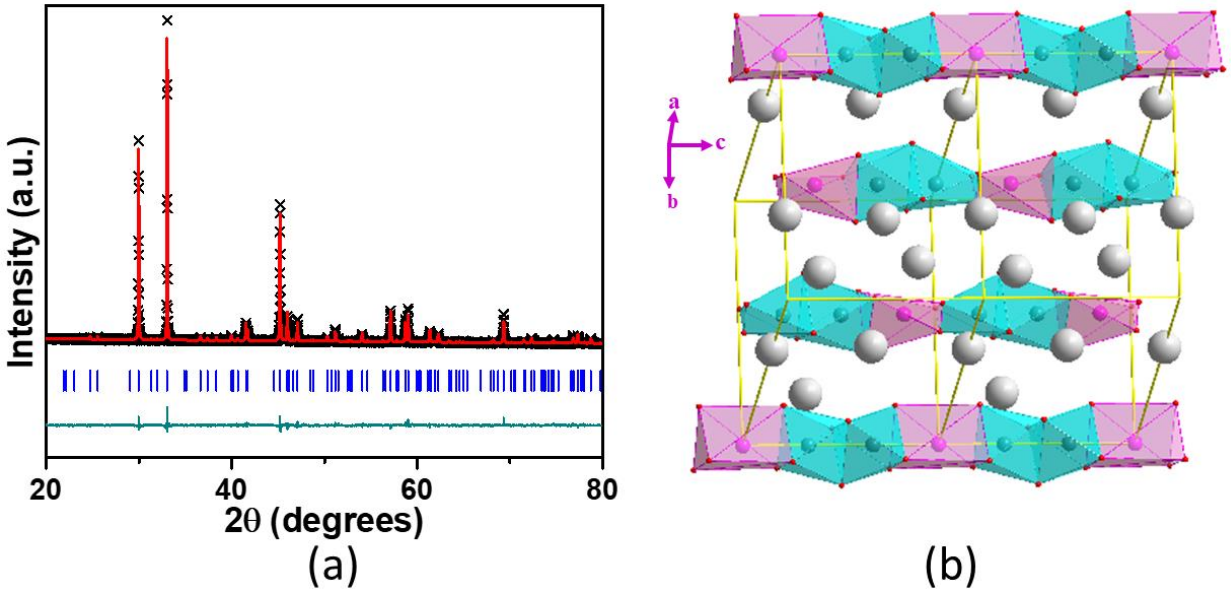

Figure 2. **(a)** Rietveld refinement profile for powder X-ray diffraction data of $Ca_2Sr_2Mn_2CoO_{10-\delta}$. Black crosses, red line, vertical tick marks and lower green line represent experimental data, the model, peak positions, and difference plot, respectively. **(b)** Crystal structure of $Ca_2Sr_2Mn_2CoO_{10-\delta}$, showing the polyhedra for Mn (turquoise) and Co (purple). Grey spheres represent Ca/Sr. Some of the polyhedral chains and Ca/Sr atoms are omitted for clarity. Yellow lines show the unit cell.

Table 2. Refined structural parameters for $Ca_2Sr_2Mn_2CoO_{10-\delta}$ using powder X-ray diffraction data. Space group *P*321, a = 9.3838(4)Å, b = 9.3838(4))Å, c = 7.7138(3)Å, V = 588.25(7)Å^3, Rp=0.0227, wRp= 0.0306, χ^2 = 2.806

Elements	x	y	z	Multiplicity	Occupancy	Uiso
Ca1/Sr1	0.020(1)	0.682(1)	0.253(2)	3	0.5/0.5	0.019(3)
Ca2/Sr2	0.341(2)	0	0.5	3	0.5/0.5	0.030(5)
Ca3/Sr3	0.3267(3)	0	0	6	0.5/0.5	0.026(5)
Mn1	0	0	0.176(3)	2	1	0.037(2)
Mn2	0.3333	0.6666	0.097(2)	2	1	0.037(2)
Mn3	0.3333	0.6666	0.356(3)	2	1	0.037(2)
Co1	0	0	0.5	2	1	0.028(3)
Co2	0.3333	0.6666	0.749(3)	1	1	0.028(3)
O1	0.499(6)	0.664(8)	0.213(5)	6	1	0.048(3)
O2	0.666(6)	0.201(4)	0.468(7)	6	1	0.048(3)
O3	0.833(8)	0	0	3	1	0.048(3)
O4	0.666(6)	0.173(6)	0.039(7)	6	1	0.048(3)
O5	0.001(6)	0.158(6)	0.273(8)	6	1	0.048(3)

Iodometric titrations show the oxygen stoichiometry of ~9 for $Ca_2Sr_2Mn_2CoO_{10-\delta}$, which implies $\delta = 1$, consistent with a previous report.[17] For $Ca_2Sr_2Mn_2FeO_{10-\delta}$, the oxygen stoichiometry was found to be ~9.5, which is nicely consistent with the replacement of Co^{2+} by Fe^{3+}. This is also consistent with the X-ray photoelectron spectroscopy data, shown in Figure 3.

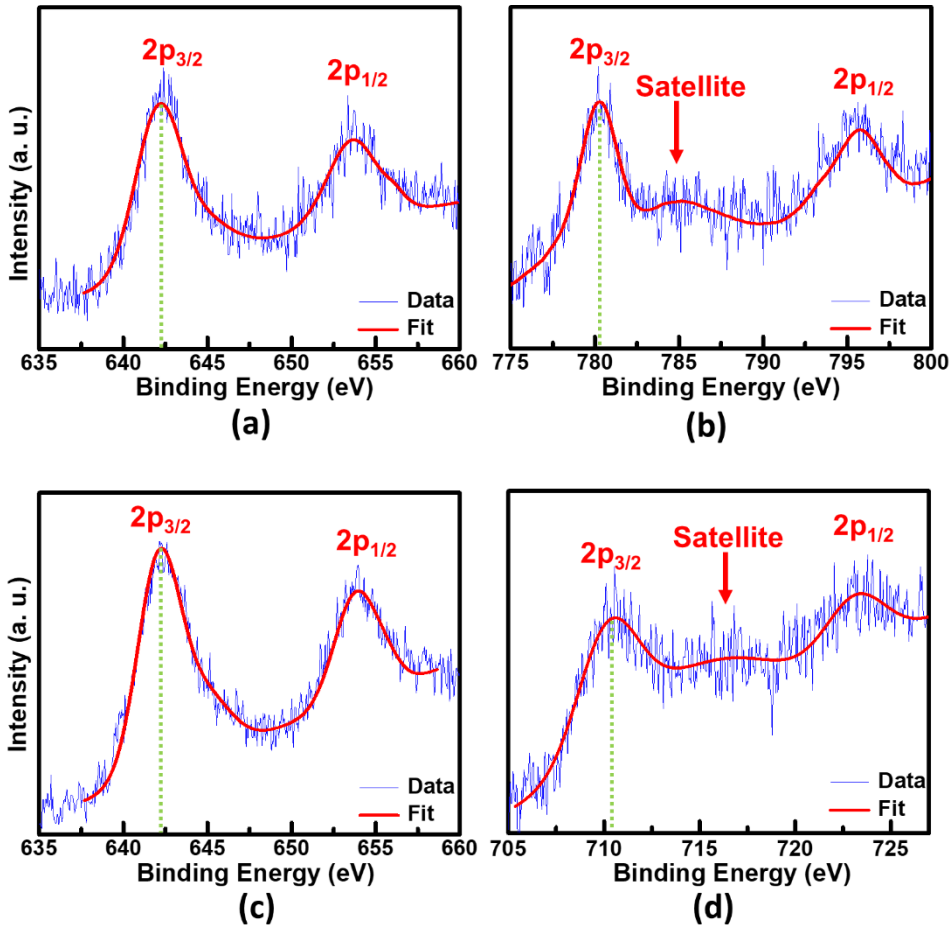

Figure 3. XPS spectra, consistent with iodometric titration results. (a) Mn spectrum for $Ca_2Sr_2Mn_2CoO_{10-\delta}$, indicating tetravalent manganese.[26,27] (b) Co spectrum for $Ca_2Sr_2Mn_2CoO_{10-\delta}$. The pronounced satellite at ~785 eV signifies divalent cobalt.[28,29] (c) Mn spectrum for $Ca_2Sr_2Mn_2FeO_{10-\delta}$, indicating tetravalent manganese.[26,27] (d) Fe spectrum for $Ca_2Sr_2Mn_2FeO_{10-\delta}$. The binding energy of $2p_{3/2}$ peak and the satellite around ~717 eV indicate trivalent iron.[29,27]

The micro-structures of the two materials are studied by high resolution scanning electron microscopy (SEM). Figure 4 shows the SEM images of sintered pellets of $Ca_2Sr_2Mn_2CoO_{10-\delta}$ and $Ca_2Sr_2Mn_2FeO_{10-\delta}$. The micrographs indicate smaller crystallites for $Ca_2Sr_2Mn_2FeO_{10-\delta}$. In addition, there appears to be a denser packing of crystallites in $Ca_2Sr_2Mn_2FeO_{9.5}$.

Overall, it is remarkable that the variation of transition metal from iron to cobalt transforms the structure from two-dimensional stacks in $Ca_2Sr_2Mn_2FeO_{10-\delta}$ to one-dimensional chains in $Ca_2Sr_2Mn_2CoO_{10-\delta}$. Importantly, this change has significant impact on electrocatalytic properties, as discussed below.

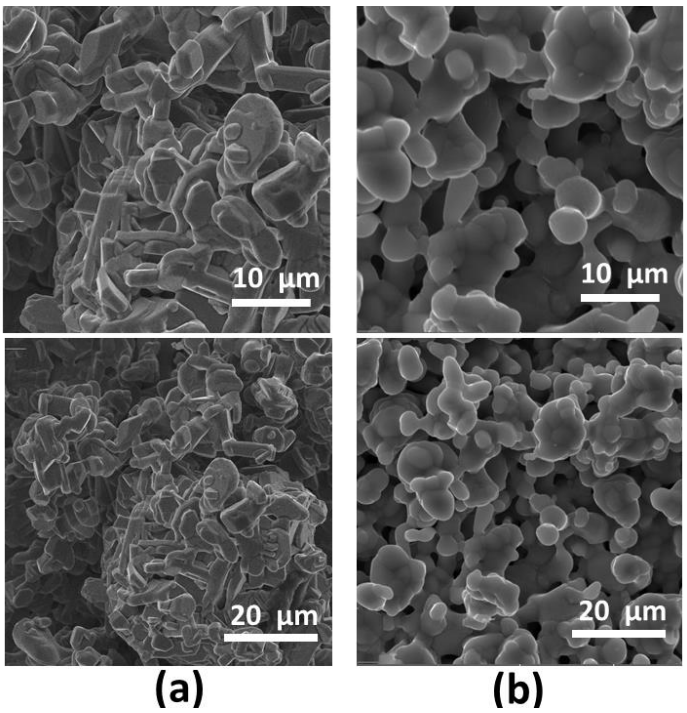

Figure 4. Scanning electron microscopy images of (a) $Ca_2Sr_2Mn_2FeO_{10-\delta}$ and (b) $Ca_2Sr_2Mn_2CoO_{10-\delta}$.

3.2. Electrocatalytic Activity for HER

Figure 5a shows the HER polarization curves of $Ca_2Sr_2Mn_2FeO_{10-\delta}$ and $Ca_2Sr_2Mn_2CoO_{10-\delta}$. Since electrocatalytic HER is commonly done in 1M KOH,[30-33] the same condition was used here to provide direct comparison to other catalysts. The electrocatalytic activity toward HER during heterogeneous catalysis is frequently gauged by the onset potential and the overpotential at 10 mA/cm^2.[34,35] The onset potential, where the HER begins (indicated by a rise in current) is almost 0.0 V versus RHE for the benchmark Pt/C (20 wt. % Pt) catalyst.[36,37]

The onset potential values for $Ca_2Sr_2Mn_2FeO_{10-\delta}$ and $Ca_2Sr_2Mn_2CoO_{10-\delta}$ are ~ –0.44 V and –0.34 V, respectively. These compounds show respective overpotential (η_{10}) values of –0.66 V and –0.45 V at –10 mA/cm^2 (Figure 5a). HER experiments were also attempted in acidic condition, 0.5 M H_2SO_4, giving overpotential of $\eta_{10} \approx 0.48$ V for $Ca_2Sr_2Mn_2CoO_{10-\delta}$, while the current response for $Ca_2Sr_2Mn_2FeO_{10-\delta}$ in this condition does not even reach 10 mA/cm^2. While oxide catalysts with better performance have been reported,[38,39] the electrocatalytic activity of $Ca_2Sr_2Mn_2CoO_{10-\delta}$ is better than some of the previously reported catalysts with Ruddlesden-Popper type structure, as shown in Table 3. This catalyst is also very stable, as shown by chronopotentiometry data in the inset of Figure 5a.

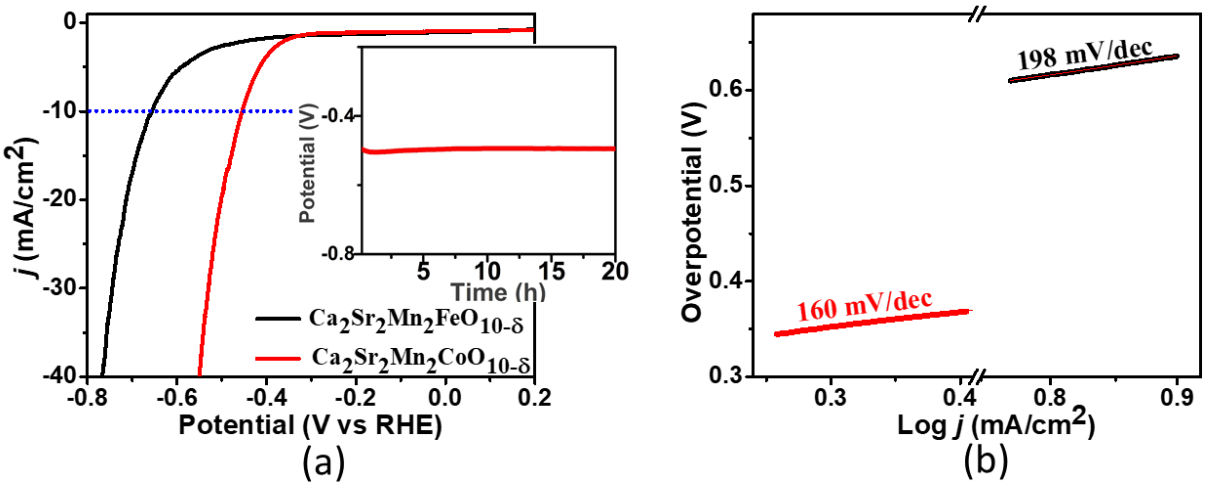

Figure 5. (a) HER polarization curves in 1 M KOH. The inset shows chronopotentiometry data, indicating the stability of $Ca_2Sr_2Mn_2CoO_{10-\delta}$. (b) Tafel plots and Tafel slopes for $Ca_2Sr_2Mn_2FeO_{10-\delta}$ (black) and $Ca_2Sr_2Mn_2CoO_{10-\delta}$ (red).

Table 3. Comparison of OER/HER overpotentials for some Ruddlesden-Popper oxides.

	OER η_{10} (mV)	HER η_{10} (mV)	Reference
$Ca_2Sr_2Mn_2CoO_{10-\delta}$	400 (0.1 M KOH)	-450 (1 M KOH)	This work
$Ca_2Sr_2Mn_2FeO_{10-\delta}$	510 (0.1 M KOH)	-660 (1 M KOH)	This work
$LaSr_3Fe_3O_{10-\delta}$	522 (0.1 M KOH)	-	[13]
$LaSr_3Co_2FeO_{10-\delta}$	475 (0.1 M KOH)	-	[13]
$LaSr_3Co_{1.5}Fe_{1.5}O_{10-\delta}$	388 (0.1 M KOH)	-	[40]
$SrLaCoO_{4-\delta}$	510 (0.1 M KOH)	-541 (1 M KOH)	[15]
$Sr_2LaCoMnO_7$	538 (0.1 M KOH)	-612 (0.5 M H_2SO_4)	[14]
$La_{0.5}Sr_{1.5}Ni_{0.7}Fe_{0.3}O_{4.04}$	360 (0.1 M KOH)	-	[41]
$Sr_3(Co_{0.8}Fe_{0.1}Nb_{0.1})_2O_{7-\delta}$	334 (0.1 M KOH)	-	[12]
$La_{1.9}Ca_{0.1}NiO_4$	>450 (0.1 M KOH)	-	[42]
Sr_2RuO_4	-	-61 (1 M KOH)	[43]

Utilizing the Tafel equation, $\eta = a + b \log j$ (where η is overpotential and j is current density), the slope of the plot of η versus $\log j$, namely Tafel slope,[44-46] is determined to evaluate the kinetics of HER (Figure 5b). Faster HER process is marked by smaller value of the Tafel slope. As shown in Figure 5b, Tafel slopes for $Ca_2Sr_2Mn_2FeO_{10-\delta}$ and $Ca_2Sr_2Mn_2CoO_{10-\delta}$ are determined to be 186 mV/dec and 154 mV/dec, respectively. A smaller Tafel slope for the latter compound indicates faster electron transfer processes, consistent with its enhanced HER activity.

3.3. Electrocatalytic Activity for OER

The electrocatalytic activity of these materials toward OER was also investigated. Figure 6a shows the OER polarization curves for $Ca_2Sr_2Mn_2FeO_{10-\delta}$ and $Ca_2Sr_2Mn_2CoO_{10-\delta}$ in 0.1M KOH electrolyte, a condition that is commonly utilized for electrocatalytic OER.[47-49] The onset potentials, marked by an increase in current, are 1.50 V and 1.40 V for $Ca_2Sr_2Mn_2FeO_{10-\delta}$ and $Ca_2Sr_2Mn_2CoO_{10-\delta}$, respectively. The onset potential of the latter compound is better than that reported for the well-known perovskite oxide electrocatalyst, $Ba_{0.5}Sr_{0.5}Co_{0.8}Fe_{0.2}O_{6-\delta}$ (BSCF), (~1.5 V). [50,51]

The overpotential (η_{10}), beyond the ideal 1.23 V, at 10 $mAcm^{-2}$ is another parameter to evaluate the OER performance.[52,53] The overpotential (η_{10}) values, obtained from $\eta_{10} = E_{RHE} - 1.23$ V, are 0.51 V and 0.40 V for $Ca_2Sr_2Mn_2FeO_{10-\delta}$ and $Ca_2Sr_2Mn_2CoO_{10-\delta}$, respectively (Figure 6a). For comparison, the η_{10} of the latter material is better than that of BSCF (~0.50 V) [54,37] and several other oxides with Ruddlesden-Popper structure, as shown in Table 3.

The OER kinetics is again evaluated using the Tafel equation $\eta = a + b \log j$,[44,55] where η is the overpotential and j is the current density. This provides information on electron and mass transport of an electrocatalyst during the OER.[56] The Tafel plot, η vs $\log j$,[39,46] is shown in Figure 6b, indicating Tafel slopes of 128 mV/dec and 86 mV/dec for $Ca_2Sr_2Mn_2FeO_{10-\delta}$, and $Ca_2Sr_2Mn_2CoO_{10-\delta}$, respectively. This is consistent with the enhanced OER activity of the latter material. In addition, this catalyst is very stable under OER conditions, as shown by the chronopotentiometry data in the inset of Figure 6a.

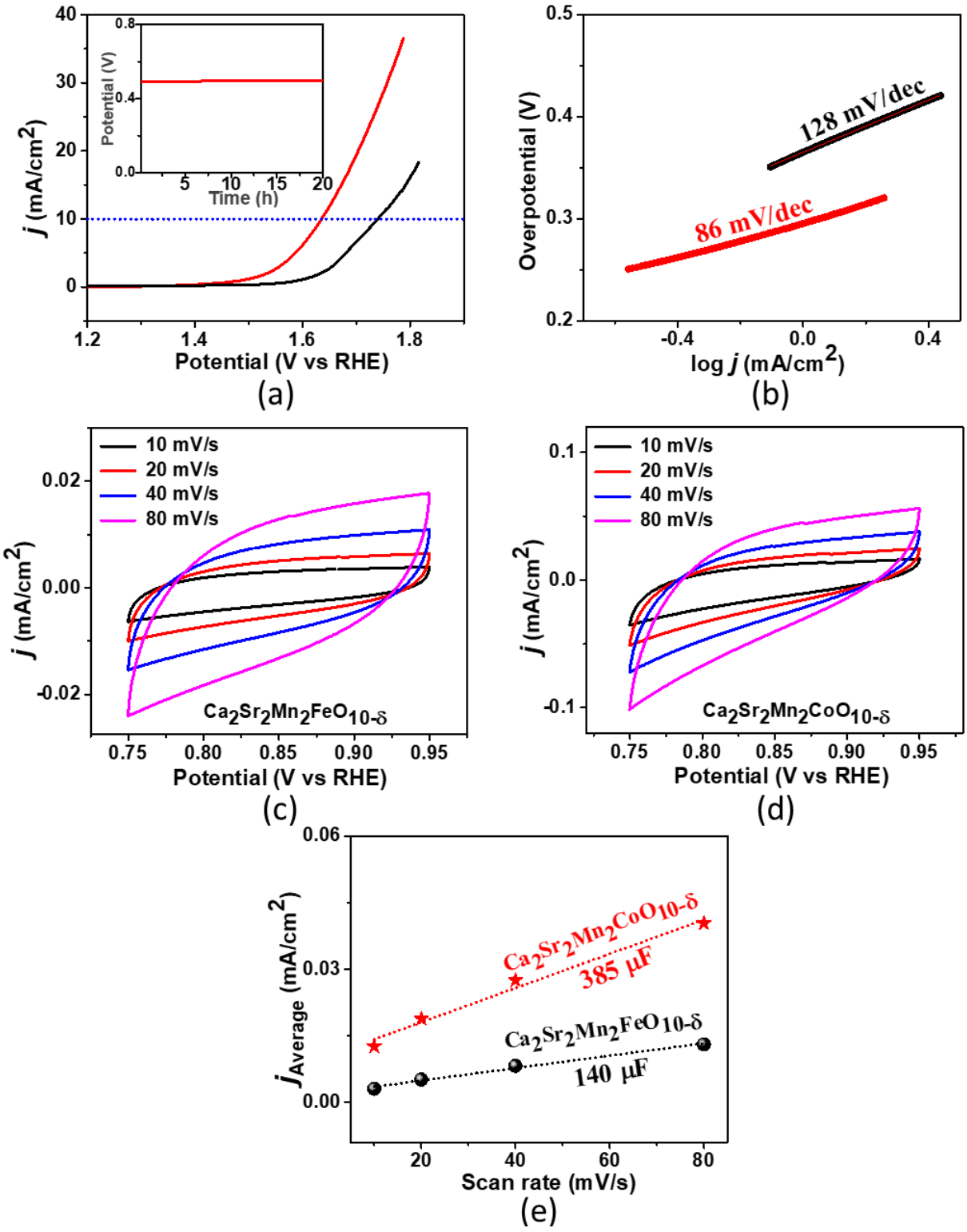

Figure 6. (a) OER polarization curves in 0.1 M KOH, for $Ca_2Sr_2Mn_2FeO_{10-\delta}$ (black) and $Ca_2Sr_2Mn_2CoO_{10-\delta}$ (red). The inset shows chronopotentiometry data, indicating the stability of $Ca_2Sr_2Mn_2CoO_{10-\delta}$. (b) Tafel plots. (c-d) Cyclic voltammetry data in non-Faradaic region. (e) Plot of $j_{average}$ versus scan rate, indicating the double layer capacitance (C_{dl}) as slope.

The electrochemically active surface area (ECSA) was also evaluated. The ECSA is commonly assessed through determination of the double layer capacitance (C_{dl}),[57,58] given the proportional relationship between ECSA and C_{dl}.[59] The C_{dl} is obtained from cyclic voltammograms collected in the non-Faradaic region (Figures 6c and 6d) based on the equation $C_{dl} = j_{average}/\nu$,[60] where $j_{average}$ is the average of the absolute values of j_{anodic} and $j_{cathodic}$ at middle potential of the CV and ν is the scan rate. Therefore, the C_{dl} value is calculated from the slope of a linear fit to $j_{average}$ versus ν.[60] As shown in Figure 6e, $Ca_2Sr_2Mn_2CoO_{10-\delta}$ shows a significantly larger C_{dl} value (385 μF) as compared to $Ca_2Sr_2Mn_2FeO_{10-\delta}$ (140 μF), consistent with the improved electrocatalytic activity of the former material.

From the above discussion on electrocatalytic activity toward HER and OER, it is evident that oxygen-vacancies and structural changes play an important role in electrocatalytic properties. As mentioned before, the δ values of ~0.5 and ~1 are confirmed from iodometric titration for $Ca_2Sr_2Mn_2FeO_{10-\delta}$ and $Ca_2Sr_2Mn_2CoO_{10-\delta}$, respectively. This is accompanied by a structural transformation from 3D in $Ca_2Sr_2Mn_2FeO_{10-\delta}$ to 1D in $Ca_2Sr_2Mn_2CoO_{10-\delta}$. The structure-property relationships have been observed in some perovskite-based oxides before.[49,61,55,62] For examples, the transformation of the crystal structure between $Sr_2Mn_2O_6$ and $CaSrMn_2O_6$ resulted in an improved OER activity for $CaSrMn_2O_6$.[61] Another study revealed the systematic trends in OER activity as a function of structure and the degree of oxygen-deficiency between $SrMnO_{2.5}$, $SrMnO_{2.6}$ and $SrMnO_3$.[49] The transformation of crystal structure between the two compounds studied in this work, $Ca_2Sr_2Mn_2FeO_{10-\delta}$ and $Ca_2Sr_2Mn_2CoO_{10-\delta}$, has a clear impact on the electrocatalytic activity. In addition, the presence of Co^{2+}, a d^7 ion, as opposed to Fe^{3+}, a d^5 ion, can have an important effect on electrocatalytic properties. It is noted that in the well-known BSCF oxide,[63] the electrocatalytic activity is primarily explained in terms of the electronic

configuration of cobalt, rather than iron. Therefore, a combination of factors, namely the type of transition metal, the oxygen stoichiometry, and the transformation of the crystal structure all lead to the enhanced properties of $Ca_2Sr_2Mn_2CoO_{10-\delta}$.

Conclusions

Changes in composition, oxygen stoichiometry, and crystal structure can all have an impact on functional properties, in particular electrocatalytic activity for water-splitting. These changes result in a significant improvement of electrocatalytic performance of $Ca_2Sr_2Mn_2CoO_{10-\delta}$ over $Ca_2Sr_2Mn_2FeO_{10-\delta}$. The latter compound exhibits superior activity toward both half-reactions of water splitting, HER and OER, as indicated by enhanced overpotential and reaction kinetics. In addition, this catalyst shows greater electrochemically active surface area and high stability in HER and OER conditions, further indicating the important impact of structural changes on functional properties.

Acknowledgements

This work is supported by the National Science Foundation (NSF) under grant no. DMR-1943085.

References

1. Alom MS, Ramezanipour F (2021) Pseudocapacitive charge storage in layered oxides $SrLaFe_{1-x}Co_xO_{4-\delta}$ (x = 0–1). Mater Lett 295:129859

2. Rossell H, Goodman P, Bulcock S, March R, Kennedy S, White T, Lincoln F, Murray K (1996) Structural and Solid-State Examination of $Ca_4Mn_3O_{10}$ and $Sr_4Mn_3O_{10}$. Aust J Chem 49:205-217. doi:https://doi.org/10.1071/CH9960205

3. Mihut AI, Spring LE, Bewley RI, Blundell SJ, Hayes W, Jestädt T, Lovett BW, McDonald R, Pratt FL, Singleton J, Battle PD, Lago J, Rosseinsky MJ, Vente JF (1998) Physical properties of then=3 Ruddlesden - Popper compound. J Phys: Condens Matter 10:L727-L735. doi:10.1088/0953-8984/10/45/001

4. Floros N, Hervieu M, van Tendeloo G, Michel C, Maignan A, Raveau B (2000) The layered manganate $Sr_{4-x}Ba_xMn_3O_{10}$: synthesis, structural and magnetic properties. Solid State Sci 2:1-9. doi:https://doi.org/10.1016/S1293-2558(00)00115-1

5. Tang Y-k, Ma X, Kou Z-q, Sun Y, Di N-l, Cheng Z-h, Li Q-a (2005) Slight La doping induced ferromagnetic clusters in layered $La_{3-3x}Sr_{1+3x}Mn_3O_{10}$ with x=1.00, 0.99. Phys RevB 72 (13):132403. doi:10.1103/PhysRevB.72.132403

6. Sannigrahi J, Chattopadhyay S, Bhattacharyya A, Giri S, Majumdar S, Venkateshwarlu D, Ganesan V (2015) Two dimensional magnetic correlation in the unconventional corrugated layered oxides $(Ba,Sr)_4Mn_3O_{10}$. J Phys: Condens Matter 27:056001. doi:10.1088/0953-8984/27/5/056001

7. Chen R, Greenblatt M, Bendersky LA (2001) Stabilization of the n = 3 Ruddlesden−Popper Phases: $Sr_4Mn_{3-x}FexO_{10-\delta}$ and $Sr_{4-y}Ca_yMn_3O_{10-\delta}$. Chem Mater 13:4094-4100. doi:10.1021/cm0102842

8. Hansteen OH, Fjellvåg H (1998) Synthesis, Crystal Structure, and Magnetic Properties of $La_4Co_3O_{10+\delta}$($0.00\leq\delta\leq0.30$). J Solid State Chem 141:212-220. doi:https://doi.org/10.1006/jssc.1998.7958

9. Olafsen A, Fjellvåg H, Hauback BC (2000) Crystal Structure and Properties of $Nd_4Co_3O_{10+\delta}$ and $Nd_4Ni_3O_{10-\delta}$. J Solid State Chem 151:46-55. doi:https://doi.org/10.1006/jssc.2000.8620

10. Chai P, Liu X, Lu M, Wang Z, Meng J (2008) Structures and Physical Properties of n = 3 Ruddlesden–Popper Compounds $Ca_4Mn_3{-}xNb_xO_{10}$ ($0 \leq x \leq 0.2$). Chem Mater 20:1988-1996. doi:10.1021/cm071712s

11. Battle PD, Branford WR, Mihut A, Rosseinsky MJ, Singleton J, Sloan J, Spring LE, Vente JF (1999) Structural Chemistry and Electronic Properties of the n = 3 Ruddlesden−Popper Phases $Ca_4Mn_2FeO_{9.75}$ and $Sr_4Mn_2FeO_{9.80}$. Chem Mater 11:674-683. doi:10.1021/cm9807384

12. Zhu Y, Tahini HA, Hu Z, Yin Y, Lin Q, Sun H, Zhong Y, Chen Y, Zhang F, Lin H-J, Chen C-T, Zhou W, Zhang X, Smith SC, Shao Z, Wang H (2020) Boosting oxygen evolution reaction by activation of lattice-oxygen sites in layered Ruddlesden-Popper oxide. EcoMat 2:e12021

13. Liu S, Sun C, Chen J, Xiao J, Luo J-L (2020) A High-Performance Ruddlesden–Popper Perovskite for Bifunctional Oxygen Electrocatalysis. ACS Catal 10:13437-13444

14. Kananke-Gamage CCW, Ramezanipour F (2021) Variation of Electrocatalytic Activity of Isostructural Oxides $Sr_2LaFeMnO_7$ and $Sr_2LaCoMnO_7$ for Hydrogen and Oxygen-Evolution Reactions. Dalton Transactions:10.1039/D1031DT01977E

15. Alom MS, Ramezanipour F (2021) Layered Oxides $SrLaFe_{1-x}Co_xO_{4-\delta}$ (x=0–1) as Bifunctional Electrocatalysts for Water-Splitting. ChemCatChem 13:3510-3516

16. Bu Y, Kim S, Kwon O, Zhong Q, Kim G (2019) A Composite Catalyst Based on Perovskites for Overall Water Splitting in Alkaline Conditions. ChemElectroChem 6:1520-1524

17. Seikh MM, Caignaert V, Perez O, Raveau B, Hardy V (2018) Interplay between single-ion magnetism, single-chain magnetism and long-range ordering in the spin chain oxides $Sr_{4-x}Ca_xMn_2CoO_9$. J MaterChem C 6:3362-3372. doi:10.1039/C7TC05968J

18. Larson AC, Von Dreele AC (1994) General structure analysis system (GSAS). Los Alamos National Laboratory Report LAUR:86 - 748

19. Toby BH (2001) A graphical user interface for GSAS. J Appl Crystallogr 34: 210−213

20. Hona RK, Ramezanipour F (2019) Enhanced electrical properties in BaSrFe2O6−δ (δ = 0.5): A disordered defect-perovskite. Polyhedron 167:69-74. doi:https://doi.org/10.1016/j.poly.2019.04.018

21. Conder K, Pomjakushina E, Soldatov A, Mitberg E (2005) Oxygen content determination in perovskite-type cobaltates. Mater Res Bull 40:257-263

22. Hona RK, Ramezanipour F (2018) Disparity in electrical and magnetic properties of isostructural oxygen-deficient perovskites $BaSrCo_2O_{6-\delta}$ and $BaSrCoFeO_{6-\delta}$. J Mater Sci Mater Electron 29:13464-13473. doi:10.1007/s10854-018-9471-8

23. Wang J, Gao Y, Chen D, Liu J, Zhang Z, Shao Z, Ciucci F (2018) Water Splitting with an Enhanced Bifunctional Double Perovskite. ACS Catal 8:364-371

24. Ng JWD, García-Melchor M, Bajdich M, Chakthranont P, Kirk C, Vojvodic A, Jaramillo TF (2016) Gold-supported cerium-doped NiO_x catalysts for water oxidation. Nat Energy 1:16053

25. Boulahya K, Parras M, González-Calbet JM, Martínez JL (2003) Synthesis, Structural Characterization, and Magnetic Study of $Sr_4Mn_2CoO_9$. Chem Mater 15:3537-3542

26. Chung YS, Kim T, Shin TH, Yoon H, Park S, Sammes NM, Kim WB, Chung JS (2017) In situ preparation of a $La_{1.2}Sr_{0.8}Mn_{0.4}Fe_{0.6}O_4$ Ruddlesden–Popper phase with exsolved Fe nanoparticles as an anode for SOFCs. J Mater Chem A 5:6437-6446

27. John F. Moulder WFS, Peter E. Sobol, Kenneth B. Bomben Handbook of X-Ray Photoelectron Spectroscopy. Perkin-Elmer Corporation, Physical Electronics Division 6509 Flying Cloud Drive Eden Prairie

28. Davison N, McWhinnie WR, Hooper A (1991) X-ray Photoelectron Spectroscopic Study of Cobalt(II) and Nickel(II) Sorbed on Hectorite and Montmorillonite. Clays and Clay Minerals 39:22-27. doi:10.1346/CCMN.1991.0390103

29. Karki SB, Ramezanipour F (2019) Magnetic and electrical properties of $BaSrMMoO_6$ (M = Mn, Fe, Co, and Ni). Mater Today Chem 13:25-33

30. Li J-S, Huang M-J, Kong L-X, Chen X-N, Zhou Y-W, Li J-L, Wang M-Y (2020) Ruthenium Nanoparticles Anchored on Graphene Hollow Nanospheres Superior to Platinum for the Hydrogen Evolution Reaction in Alkaline Media. Inorg Chem 59:930-936

31. Shi M, Zhang Y, Zhu Y, Wang W, Wang C, Yu A, Pu X, Zhai J (2020) A flower-like CoS_2/MoS_2 heteronanosheet array as an active and stable electrocatalyst toward the hydrogen evolution reaction in alkaline media. RSC Adv 10:8973-8981

32. Razmjooei F, Liu T, Azevedo DA, Hadjixenophontos E, Reissner R, Schiller G, Ansar SA, Friedrich KA (2020) Improving plasma sprayed Raney-type nickel–molybdenum electrodes towards high-performance hydrogen evolution in alkaline medium. Sci Rep 10:10948

33. Ma L, Ting LRL, Molinari V, Giordano C, Yeo BS (2015) Efficient hydrogen evolution reaction catalyzed by molybdenum carbide and molybdenum nitride nanocatalysts synthesized via the urea glass route. J Mater Chem A 3:8361-8368

34. Hwang BJ, Chen HC, Mai FD, Tsai HY, Yang CP, Rick J, Liu YC (2015) Innovative Strategy on Hydrogen Evolution Reaction Utilizing Activated Liquid Water. Sci Rep 5:16263

35. Mohammed-Ibrahim J, Sun X (2019) Recent progress on earth abundant electrocatalysts for hydrogen evolution reaction (HER) in alkaline medium to achieve efficient water splitting – A review. J Energy Chem 34:111-160

36. Zhu Y, Zhou W, Zhong Y, Bu Y, Chen X, Zhong Q, Liu M, Shao Z (2017) A Perovskite Nanorod as Bifunctional Electrocatalyst for Overall Water Splitting. Adv Energy Mater 7:1602122

37. Xu X, Chen Y, Zhou W, Zhu Z, Su C, Liu M, Shao Z (2016) A Perovskite Electrocatalyst for Efficient Hydrogen Evolution Reaction. Adv Mater 28:6442-6448

38. Sun Q, Dai Z, Zhang Z, Chen Z, Lin H, Gao Y, Chen D (2019) Double perovskite $PrBaCo_2O_{5.5}$: An efficient and stable electrocatalyst for hydrogen evolution reaction. J Power Sources 427:194-200

39. Hona RK, Karki SB, Ramezanipour F (2020) Oxide Electrocatalysts Based on Earth-Abundant Metals for Both Hydrogen- and Oxygen-Evolution Reactions. ACS Sustainable Chem Eng 8:11549-11557. doi:10.1021/acssuschemeng.0c02498

40. Liu S, Luo H, Li Y, Liu Q, Luo J-L (2017) Structure-engineered electrocatalyst enables highly active and stable oxygen evolution reaction over layered perovskite $LaSr_3Co_{1.5}Fe_{1.5}O_{10-\delta}$. Nano Energy 40:115-121

41. Forslund RP, Hardin WG, Rong X, Abakumov AM, Filimonov D, Alexander CT, Mefford JT, Iyer H, Kolpak AM, Johnston KP, Stevenson KJ (2018) Exceptional electrocatalytic oxygen evolution via tunable charge transfer interactions in $La_{0.5}Sr_{1.5}Ni_{1-x}Fe_xO_{4\pm\delta}$ Ruddlesden-Popper oxides. Nat Commun 9:3150

42. Jung K-N, Jung J-H, Im WB, Yoon S, Shin K-H, Lee J-W (2013) Doped Lanthanum Nickelates with a Layered Perovskite Structure as Bifunctional Cathode Catalysts for Rechargeable Metal–Air Batteries. ACS Appl Mater Interfaces 5:9902-9907

43. Zhu Y, Tahini HA, Hu Z, Dai J, Chen Y, Sun H, Zhou W, Liu M, Smith SC, Wang H, Shao Z (2019) Unusual synergistic effect in layered Ruddlesden−Popper oxide enables ultrafast hydrogen evolution. Nat Commun 10:149

44. Allen J. Bard LRF Electrochemical Methods: Fundamentals and Applications. 2, illustrated edn. Wiley, 2000,

45. Karki SB, Ramezanipour F (2020) Pseudocapacitive Energy Storage and Electrocatalytic Hydrogen-Evolution Activity of Defect-Ordered Perovskites $Sr_xCa_{3-x}GaMn_2O_8$ (x = 0 and 1). ACS Appl Energy Mater. doi:10.1021/acsaem.0c01935

46. Shinagawa T, Garcia-Esparza AT, Takanabe K (2015) Insight on Tafel slopes from a microkinetic analysis of aqueous electrocatalysis for energy conversion. Sci Rep 5:13801-13801

47. Kumar N, Kumar M, Nagaiah TC, Siruguri V, Rayaprol S, Yadav AK, Jha SN, Bhattacharyya D, Paul AK (2020) Investigation of New B-Site-Disordered Perovskite Oxide $CaLaScRuO_{6+\delta}$: An Efficient Oxygen Bifunctional Electrocatalyst in a Highly Alkaline Medium. ACS Appl Mater Interfaces 12:9190-9200

48. Xu W, Apodaca N, Wang H, Yan L, Chen G, Zhou M, Ding D, Choudhury P, Luo H (2019) A-site Excessive $(La_{0.8}Sr_{0.2})_{1+x}MnO_3$ Perovskite Oxides for Bifunctional Oxygen Catalyst in Alkaline Media. ACS Catal 9:5074-5083

49. Hona RK, Ramezanipour F (2020) Effect of the Oxygen Vacancies and Structural Order on the Oxygen Evolution Activity: A Case Study of $SrMnO_{3-\delta}$ Featuring Four Different Structure Types. Inorg Chem 59:4685-4692

50. Chen G, Zhou W, Guan D, Sunarso J, Zhu Y, Hu X, Zhang W, Shao Z (2017) Two orders of magnitude enhancement in oxygen evolution reactivity on amorphous $Ba_{0.5}Sr_{0.5}Co_{0.8}Fe_{0.2}O_{3-\delta}$ nanofilms with tunable oxidation state. Sci Adv 3:e1603206

51. Chaitoglou S, Bertran E (2017) Effect of temperature on graphene grown by chemical vapor deposition. J Mater Sci 52:8348-8356. doi:10.1007/s10853-017-1054-1

52. Chang C, Zhu S, Liu X, Chen Y, Sun Y, Tang Y, Wan P, Pan J (2021) One-Step Electrodeposition Synthesis of Bimetal Fe- and Co-Doped NiPi/P for Highly Efficient Overall Water Splitting. Ind Eng Chem Res 60:2070-2078

53. Tong X, Yang P, Wang Y, Qin Y, Guo X (2014) Enhanced photoelectrochemical water splitting performance of TiO_2 nanotube arrays coated with an ultrathin nitrogen-doped carbon film by molecular layer deposition. Nanoscale 6:6692-6700

54. Zhu Y, Zhou W, Chen Z-G, Chen Y, Su C, Tadé MO, Shao Z (2015) $SrNb_{0.1}Co_{0.7}Fe_{0.2}O_{3-\delta}$ Perovskite as a Next-Generation Electrocatalyst for Oxygen Evolution in Alkaline Solution. Angew Chem 54:3897-3901

55. Hona RK, Ramezanipour F (2019) Remarkable Oxygen-Evolution Activity of a Perovskite Oxide from the $Ca_{2-x}Sr_xFe_2O_{6-\delta}$ Series. Angew Chem 58:2060-2063. doi:10.1002/anie.201813000

56. Moir J, Soheilnia N, O'Brien P, Jelle A, Grozea CM, Faulkner D, Helander MG, Ozin GA (2013) Enhanced Hematite Water Electrolysis Using a 3D Antimony-Doped Tin Oxide Electrode. ACS Nano 7:4261-4274. doi:10.1021/nn400744d

57. Wei C, Rao RR, Peng J, Huang B, Stephens IEL, Risch M, Xu ZJ, Shao-Horn Y (2019) Recommended Practices and Benchmark Activity for Hydrogen and Oxygen Electrocatalysis in Water Splitting and Fuel Cells. Adv Mater 31:1806296

58. Lee JG, Hwang J, Hwang HJ, Jeon OS, Jang J, Kwon O, Lee Y, Han B, Shul Y-G (2016) A New Family of Perovskite Catalysts for Oxygen-Evolution Reaction in Alkaline Media: $BaNiO_3$ and $BaNi_{0.83}O_{2.5}$. J Am Chem Soc 138:3541-3547. doi:10.1021/jacs.6b00036

59. Pan Y, Chen Y, Li X, Liu Y, Liu C (2015) Nanostructured nickel sulfides: phase evolution, characterization and electrocatalytic properties for the hydrogen evolution reaction. RSC Adv 5:104740-104749. doi:10.1039/C5RA18737K

60. Petrie JR, Cooper VR, Freeland JW, Meyer TL, Zhang Z, Lutterman DA, Lee HN (2016) Enhanced Bifunctional Oxygen Catalysis in Strained $LaNiO_3$ Perovskites. J Am Chem Soc 138:2488-2491

61. Hona RK, Ramezanipour F (2019) Structure-dependence of electrical conductivity and electrocatalytic properties of $Sr_2Mn_2O_6$ and $CaSrMn_2O_6$. J Chem Sci 131:109

62. Kim J, Yin X, Tsao K-C, Fang S, Yang H (2014) $Ca_2Mn_2O_5$ as Oxygen-Deficient Perovskite Electrocatalyst for Oxygen Evolution Reaction. J Am Chem Soc 136:14646-14649. doi:10.1021/ja506254g

63. Suntivich J, May KJ, Gasteiger HA, Goodenough JB, Shao-Horn Y (2011) A Perovskite Oxide Optimized for Oxygen Evolution Catalysis from Molecular Orbital Principles. Science 334:1383. doi:10.1126/science.1212858

Table of Contents

Ruddlesden-Popper structure of $Ca_2Sr_2Mn_2FeO_{10-\delta}$ transform to a 1D structure in $Ca_2Sr_2Mn_2CoO_{10-\delta}$. The latter shows significant enhancement of electrocatalytic properties for both half reactions of water-splitting, namely oxygen-evolution and hydrogen-evolution reactions.